

Article

Effect of Bismuth on the Structure, Magnetic and Photocatalytic Characteristics of $GdFeO_3$

Yudie Ma, Hui Shen , Yating Fang, Heyan Geng, Yu Zhao, Yasheng Li, Jiayue Xu and Yunfeng Ma

Institute of Crystal Growth, School of Materials Science and Engineering, Shanghai Institute of Technology, Shanghai 201418, China

* Correspondence: hshen@sit.edu.cn

Abstract: In this paper, a series of $Gd_{1-x}Bi_xFeO_3$ ($x = 0, 0.1, 0.3, 0.5, 0.7, 0.9, 1$) nanoparticles have been readily synthesized by a green and facile sol-gel method. It gradually changed from the orthorhombic structure (space group $Pbnm$) to the rhombohedral perovskite structure (space group $R3c$). Weak ferromagnetic behavior was effectively induced by Bi^{3+} , with reduced magnetization. It was closely related with the lattice distortion of the perovskite structure and modified interactions between Fe-O-Fe. Boosted photocatalytic activities of $Gd_{1-x}Bi_xFeO_3$ were observed for the removal of methylene blue (MB) under the visible light irradiation. In particular, $Gd_{0.5}Bi_{0.5}FeO_3$ showed the optimum photocatalytic efficiency, in which the degradation efficiency reached 82.1% after 180 min of visible light illumination, with good stability and repeatability. The improved performance was mainly ascribed to enhanced visible light absorption, decreased optical band gap from 2.21 to 1.8eV and stronger charge transfer efficiency. A possible photocatalytic mechanism is also proposed according to the band structure. The results indicate that this system will be a promising candidate for the degradation of organic pollutant as a novel magnetically recoverable photocatalyst.

Keywords: perovskite; orthoferrites; sol-gel; magnetic; photocatalysis



Citation: Ma, Y.; Shen, H.; Fang, Y.; Geng, H.; Zhao, Y.; Li, Y.; Xu, J.; Ma, Y. Effect of Bismuth on the Structure, Magnetic and Photocatalytic Characteristics of $GdFeO_3$. *Magnetochemistry* **2023**, *9*, 45. <https://doi.org/10.3390/magnetochemistry9020045>

Academic Editor: Andrea Caneschi

Received: 25 November 2022

Revised: 20 January 2023

Accepted: 27 January 2023

Published: 29 January 2023



Copyright: © 2023 by the authors. Licensee MDPI, Basel, Switzerland. This article is an open access article distributed under the terms and conditions of the Creative Commons Attribution (CC BY) license (<https://creativecommons.org/licenses/by/4.0/>).

1. Introduction

The rare earth orthoferrite ($RFeO_3$) with perovskite structure has received intensive attention, thanks to its exotic magnetism, multiferroics and unique features for fast magneto-optical isolator, ultra-fast spin switching, etc. [1]. Moreover, due to the suitable band gap, $RFeO_3$ has also been considered as a potential visible light photocatalyst for the degradation of organic pollutants [2–4]. Interestingly, these magnetic photocatalysts display advantages of magnetic separation and recyclability after photocatalytic reactions, which make them easy to recover from waste water to avoid secondary pollution. As a typical orthoferrite compound, $GdFeO_3$ contains Gd^{3+} half-filled 4f shell and a stable structure with a $Pbnm$ space group. It displays a narrow band gap (around 2.4 eV), capable of absorbing both visible and UV light. Some studies have been conducted to investigate the photocatalytic behaviors of $GdFeO_3$, and effective strategies have also been proposed to boost the photocatalytic performance. For instance, the substitution of Mn at the Fe site of $GdFeO_3$ introduces an extra electronic state between the conduction band and the valence band, which reduces the optical band gap and enhances the rhodamine-B (Rh-B) degradation efficiency [5]. The degradation rate of Rh-B is greatly improved by a factor of 2.5 for $GdFe_{0.7}Mn_{0.3}O_3$ as compared to pure $GdFeO_3$. Similarly, the introduction of Mn in $ErFeO_3$ greatly increases the photocatalytic degradation efficiency of methylene blue (MB), due to the narrower band gap and smaller particle size [6]. Moreover, the degradation efficiency of Rh-B up to 92% at 120 min is achieved in $GdFeO_3/g-C_3N_4$ -3:7 composites, while minor weight loss is observed during the consecutive runs [7].

Bismuth ferrites ($BiFeO_3$), with distorted rhombohedral perovskite structure, shows fascinating multiferroic properties with simultaneous antiferromagnetic ordering ($T_N = 370$ °C) and

ferroelectric configurations ($T_c = 830\text{ }^\circ\text{C}$) at room temperature [8]. BiFeO_3 is also regarded as a novel photocatalyst under visible light irradiation, owing to its narrow band gap (2.0 eV–2.2 eV) and excellent chemical stability [9,10]. Meanwhile, the internal electric field from ferroelectric BiFeO_3 possibly enhances surface reactions and photogenerated charge separation efficiency [11]. However, the photocatalytic performance is still restricted by the presence of impurity phases, structural instability, and slow mobility rate [12]. Various strategies have also been applied to boost the photocatalytic efficiency, such as surface engineering, morphology tuning, heterostructure formation, doping and crystal facet engineering. For example, La-doped BiFeO_3 -based multiferroics were synthesized to achieve a strong magnetic response and high piezo-photocatalytic activity [12]. The optical bandgap of BiFeO_3 nanoparticles has been tuned from 2.06 eV to 1.75 eV by Cd-Ni co-doping. The best degradation activity of MB and Rh-B has been achieved in a $\text{Bi}_{0.94}\text{Cd}_{0.06}\text{Fe}_{0.94}\text{Ni}_{0.06}\text{O}_3$ sample under UV–visible irradiation, which may be originated from the high surface area, smaller average particle size and bandgap [8]. MB dye was almost completely degraded in 120 min for a $\text{AgFe}_2\text{O}_4/\text{BiFeO}_3$ heterostructure under visible light irradiation [13].

Now, enhanced photocatalytic performance of ferrites is still highly expected by effective regulation of the structure, morphology, band energy, etc. Dopants are proven to be feasible strategies to modify the magnetic and photocatalytic properties of orthoferrites. Substituents may act as surface traps for holes and electrons, reducing recombination rate and increasing photo-produced charge carrier lifetime, leading to enhanced photocatalysis of materials [11]. The lattice structure, electronic band gap and the dipole–dipole interaction of perovskites can also be effectively regulated by the substitution at the A site or B site, making it possible to effectively modulate the optical, magnetic, electrical and catalytic properties. Orthorhombic GdFeO_3 and rhombohedral BiFeO_3 show distinctive crystal structures. Cation substitution of Gd^{3+} for larger Bi^{3+} cations results in structural modifications mainly in FeO_6 rotations and tilting, and the electric polar moment on GdFeO_3 is also modified by the s^2 lone pairs of electrons in the Bi cations [14]. Therefore, the influence of Bi^{3+} on the lattice structure, band energy, magnetic properties and catalytic behaviors of GdFeO_3 need to be explored. Recently, it has been reported that the introduction of Bi^{3+} in YFeO_3 does not generate significant changes in band gap values and photocatalytic efficiency, but modifies the crystal structure and the magnetic behavior [14]. The investigation towards the effect of Bi^{3+} on the structure, magnetic and photocatalytic characteristics of GdFeO_3 is still scarce. Herein, a series of $\text{Gd}_{1-x}\text{Bi}_x\text{FeO}_3$ ($x = 0, 0.1, 0.3, 0.5, 0.7, 0.9, 1$) powders were prepared by the sol–gel method. Sponge-like particles are usually formed during the sol–gel method, which is helpful for enhancing the catalytic reactions. The crystal structure, crystalline morphology, magnetic and optical properties of the as-prepared samples were fully characterized. The photocatalytic activity of the samples was investigated via the degradation of MB under visible light irradiation. The photocatalytic efficiency was effectively increased by the introduction of Bi^{3+} . The optimum catalytic performance was observed for $\text{Gd}_{0.5}\text{Bi}_{0.5}\text{FeO}_3$, which was mainly ascribed to the narrower band gap, increased optical absorption, and enhanced charge transfer efficiency.

2. Materials and Methods

A series of $\text{Gd}_{1-x}\text{Bi}_x\text{FeO}_3$ ($x = 0, 0.1, 0.3, 0.5, 0.7, 0.9, 1$ marked as GFO, GBFO1, GBFO3, GBFO5, GBFO7, GBFO9, BFO) powders were been readily synthesized by the sol–gel method. The raw materials were $\text{Gd}(\text{NO}_3)_3 \cdot 6\text{H}_2\text{O}$ (99%), $\text{Fe}(\text{NO}_3)_3 \cdot 9\text{H}_2\text{O}$ (99%) and $\text{Bi}(\text{NO}_3)_3 \cdot 5\text{H}_2\text{O}$ (99%), and citric acid was chosen as the complexing agent. First, at the appropriate stoichiometric ratio, $\text{Gd}(\text{NO}_3)_3 \cdot 6\text{H}_2\text{O}$, $\text{Fe}(\text{NO}_3)_3 \cdot 9\text{H}_2\text{O}$ and $\text{Bi}(\text{NO}_3)_3 \cdot 5\text{H}_2\text{O}$ were dissolved in deionized water to form a transparent solution. Then, the appropriate amount of citric acid was added into the solution. Second, the pH of the solution was adjusted to 1–2 by adding an ammonia solution. The solution was magnetically stirred at about $80\text{ }^\circ\text{C}$ until a sticky gel was formed. Subsequently, the sticky gel was ignited at a setting temperature of $300\text{ }^\circ\text{C}$. Thereafter, the samples were calcined at different temperatures ($550\text{ }^\circ\text{C}$ – $700\text{ }^\circ\text{C}$) in air for 3 h.

The phase identification and crystal structures were checked by X-ray diffraction (XRD, D/Max-2550V, Rigaku, Tokyo, Japan) in the 2θ range of 10° to 80° with a step scanning of 0.02° per step to identify the phase and to calculate the lattice parameters. The Rietveld refinements of the XRD patterns were conducted by the GSAS program. The morphology and microstructure of the prepared samples were investigated by scanning electron microscopy (SEM, S4800, Hitachi, Chiyoda-ku, Japan). The surface composition and valence states of Bi, Fe and O were determined by X-ray photoelectron spectroscopy (XPS, Thermo Scientific K-Alpha, Thermo Fisher Scientific, Waltham, MA, USA) with $AlK\alpha$ as the radiation source ($h\nu = 1486.6$ eV). The magnetic properties of the samples were studied by a vibrating sample magnetometer (VSM, Lakeshore7407, Lakeshore, Columbus, OH, USA). UV-vis absorption spectra of the samples were recorded with an UV-vis spectrophotometer (Cary 5000, Agilent Technologies, Santa Clara, CA, USA).

The photocatalytic activity of all the samples was evaluated by photodegradation of MB using visible light irradiation with a xenon lamp (500 W) with a 420 nm cutoff filter as a light source at room temperature. A total of 50 mg of photocatalyst was added to 50 mL of methylene blue (MB) solution with a concentration of 5 mg/L. Prior to the visible light irradiation, the reaction mixture was homogeneously stirred in the dark for 60 min to attain the adsorption–desorption equilibrium. The solution of the sample was positioned 20 cm away from the xenon lamp. Then, the solution was exposed to light with continuous stirring; at regular 20–30 min intervals, about 3 mL of solution was collected and centrifuged to remove the catalyst particles. The photocatalytic activities of the synthesized $Gd_{1-x}Bi_xFeO_3$ were monitored by the change in the concentration of MB, which was evaluated by the variation of absorption band maximum (664 nm) using a UV-vis spectrophotometer. Electrochemical impedance spectroscopy (EIS) and Mott–Schottky (MS) curves were carried out on an electrochemical workstation (CHI 760E, CH Instrument, Shanghai Chenhua Instrument Company, Shanghai, China) using a three-electrode system. The saturated Ag/AgCl and platinum foil served as the reference electrode and the counter electrode, respectively. The working electrode was prepared by dip-coating the slurry (5 mg of photocatalyst powders dispersed in 50 μ L of ethanol and 10 μ L of Nafion solution (5 wt%) under sonication) on the FTO glass. A 0.1 M Na_2SO_4 aqueous solution (pH 6.8) was used as the electrolyte. EIS tests were recorded under visible light ($\lambda \geq 400$ nm) irradiation by applying an AC voltage of 5 mV in the frequency range from 0.01 Hz to 100 kHz. The Mott–Schottky plots were measured with a fixed frequency of 2000 Hz.

3. Results

$Gd_xBi_{1-x}FeO_3$ ($x = 0, 0.1, 0.3, 0.5, 0.7$) samples were prepared and calcined at $700^\circ C$, while $Gd_xBi_{1-x}FeO_3$ ($x = 0.9, 1$) powders were successfully obtained at $550^\circ C$. The results indicate that Bi^{3+} is effective in lowering the formation temperature of orthoferrite, without any observable impurities. The Rietveld refined X-ray powder diffraction patterns of $Gd_xBi_{1-x}FeO_3$ are shown in Figure 1. In Figure 1a, when the content of Bi^{3+} was ≤ 0.5 , the pure orthorhombic perovskite phase ($GdFeO_3$, PDF No. 74-1476) was observed, without any impurities. Obviously, the mixed phase of the $Pnma$ (wt $\approx 64.68\%$) and $R3c$ (wt $\approx 35.32\%$) phase was observed at $x = 0.7$, indicating that the orthorhombic perovskite structure can remain when the content of bismuth was lower than $x = 0.7$. Figure 1b reveals an enlarged view of the (112) diffraction peak around 32° and 34° . As the Bi concentration increased, this diffraction peak shifted towards a lower 2θ value, suggesting enlarged lattice volumes. In Figure 1c, when the concentration of Bi^{3+} was ≥ 0.9 , the pure rhombohedral perovskite ($R3c$) ($BiFeO_3$, PDF No. 72-2112) was obtained. The phase transition was attributed to the structural distortion resulting from the incorporation of Bi^{3+} ions into the lattice of GFO, since the ionic radius of Bi^{3+} (1.17 Å) is larger than of Gd^{3+} (1.05 Å) [15]. Lattice distortion will cause changes in the lattice parameters, bond length, bond angle of Fe–O–Fe and other related parameters.

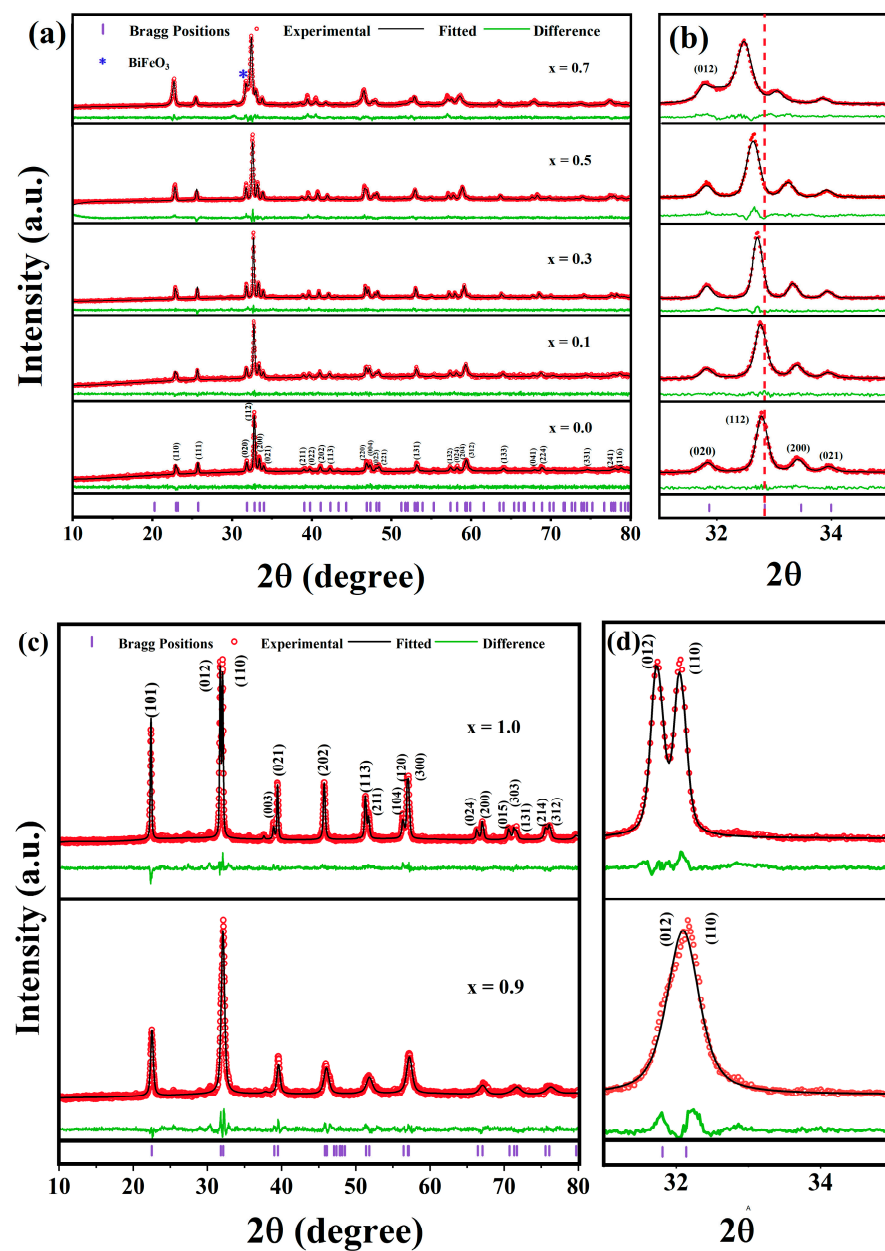


Figure 1. XRD patterns of (a) $\text{Gd}_{1-x}\text{Bi}_x\text{FeO}_3$ ($x = 0, 0.1, 0.3, 0.5, 0.7$) annealed at $700\text{ }^\circ\text{C}$; (c) $\text{Gd}_{1-x}\text{Bi}_x\text{FeO}_3$ ($x = 0.9, 1.0$) annealed at $550\text{ }^\circ\text{C}$; (b,d) enlarged view of 2θ from 31° to 35° .

Table 1 shows the refined unit cell parameters, bond angle, bond length and goodness of fit. For the samples of $\text{Gd}_x\text{Bi}_{1-x}\text{FeO}_3$ ($x = 0, 0.1, 0.3, 0.5$), the lattice parameters of the *Pnma* phase gradually increased with the increased concentration of Bi^{3+} , suggesting the component-driven structural distortions. For the samples of $\text{Gd}_x\text{Bi}_{1-x}\text{FeO}_3$ ($x = 0.7, 0.9, 1$) in the *R3c* phase, the lattice constants *a* and *b* decreased with the increase in Bi content while the lattice constant *c* increased with the increase in Bi. Overall, the unit volumes were enlarged with the introduction of Bi for these samples. Additionally, the change of the bond length and the bond angles were varied for the *Pnma* phase and the *R3c* phase. In particular, for GBFO5, the Fe-O1 bond length and the Fe-O2 bond length were expanded to 2.043 \AA and 2.033 \AA , respectively, while the bond angles of Fe-O1-Fe and Fe-O2-Fe were increased to be 142.943° and 146.985° , respectively. Moreover, it has been reported that the hybridization between Bi and O could possibly induce enhanced octahedral tilting distortion of the perovskite structure [16].

Table 1. Refined structural parameters for Gd_{1-x}Bi_xFeO₃ (x = 0, 0.1, 0.3, 0.5, 0.7, 0.9, 1.0) samples.

		GFO	GBFO1	GBFO3	GBFO5	GBFO7		GBFO9	BFO
Space Group		<i>Pbmm</i>	<i>Pbmm</i>	<i>Pbmm</i>	<i>Pbmm</i>	<i>Pbmm</i> (Wt: 64.68%)	<i>R3c</i> (Wt: 35.32%)	<i>R3c</i>	<i>R3c</i>
Lattice parameters	a (Å)	5.321 (3)	5.349 (3)	5.373 (3)	5.394 (3)	5.398 (3)	5.635 (3)	5.598 (3)	5.578 (3)
	b (Å)	5.578 (3)	5.605 (3)	5.620 (3)	5.629 (3)	5.609 (3)	5.635 (3)	5.598 (3)	5.578 (3)
	c (Å)	7.632 (3)	7.673 (3)	7.711 (3)	7.747 (3)	7.753 (3)	13.503 (3)	13.723 (3)	13.865 (3)
	V (Å ³)	226.568 (0)	230.062 (0)	232.846 (0)	235.243 (0)	234.774 (0)	371.327 (0)	372.387 (0)	373.544 (0)
	α = β	90°	90°	90°	90°	90°	90°	90°	90°
	γ	90°	90°	90°	90°	90°	120°	120°	120°
Bond length	Gd/Bi-O1 (Å)	2.264 (20)	2.275 (19)	2.283 (11)	2.290 (7)	2.287 (19)	2.292 (29)	2.304 (18)	2.312 (37)
	Gd/Bi-O2 (Å)	2.505 (16)	2.518 (15)	2.528 (9)	2.538 (5)	2.537 (14)	2.539 (5)	2.526 (14)	2.519 (6)
	Fe-O1 (Å)	2.013 (14)	2.024 (13)	2.033 (8)	2.0425 (6)	2.044 (18)	2.023 (26)	2.023 (13)	2.025 (35)
	Fe-O2 (Å)	2.010 (14)	2.020 (14)	2.027 (8)	2.033 (5)	2.030 (13)			
Bond angle	Fe-O1-Fe (°)	142.881 (3)	142.888 (3)	142.910 (2)	142.943 (12)	142.968 (4)	156.087 (1)	156.156 (3)	156.200 (1)
	Fe-O2-Fe (°)	147.042 (1)	147.037 (1)	147.015 (1)	146.985 (5)	146.947 (2)			
Other parameter	density (g·cm ⁻³)	7.654	7.538	7.448	7.372		7.387	8.394	8.369
Statistical fit	χ ²	1.152	1.039	1.394	3.179		1.862	1.981	1.78
	wRp (%)	4.80	4.74	5.86	9.44		7.64	8.45	8.48
	Rp (%)	3.82	3.74	4.51	6.21		5.94	6.78	6.52

Figure 2a–d shows the SEM images of the prepared Gd_{1-x}Bi_xFeO₃ (x = 0, 0.5, 0.7, 0.9) powders. The Gd_{1-x}Bi_xFeO₃ (x = 0, 0.5, 0.7) samples were calcined at 700 °C and Gd_{0.1}Bi_{0.9}FeO₃ was prepared at 550 °C. The statistical calculation of the grain size distribution of the corresponding samples is shown in Figure 2e–h. In Figure 2a, pure GFO particles were highly agglomerated and the crystalline grains were well defined by the grain boundaries, which showed irregular shapes with an average grain size around 190 nm. The continuous porous network was attributed from the releasing of a large amount of gas during the combustion reaction process. Plate-like particles were observed for Gd_{0.5}Bi_{0.5}FeO₃, as seen in Figure 2b, with an average particle size around 123 nm. Figure 2c shows the SEM images of the prepared Gd_{0.3}Bi_{0.7}FeO₃ powder, with a grain size of about 180 nm. Apparently, with increasing doping amounts, the grain size of the samples decreased gradually, indicating that the crystal growth was inhibited by the introduction of Bi³⁺. This behavior could be attributed to the formation of crystal defects due to the occupation of the lattice site of the host structure by dopant ions, which acts as a barrier to the crystal growth and thus reduces the particle size [17]. Figure 2d shows the SEM images of the Gd_{0.1}Bi_{0.9}FeO₃ powder calcined at 550 °C. Due to the lower calcination temperature, the elliptical or spherical particles were partially agglomerated, with a particle size of around 120 nm. Smaller particles had a higher surface energy, which may stimulate the agglomeration process to occur [18].

Figure 3 demonstrates the result of the XPS analysis of the spectra of the elements Bi, Fe and O in the Gd_{0.5}Bi_{0.5}FeO₃ sample. Figure 3a shows the two peaks located at 158.68 eV for Bi 4f_{7/2} and 163.98 eV for Bi 4f_{5/2}. The energy difference between the Bi 4f_{7/2} and Bi 4f_{5/2} peaks was around 5.3 eV, which confirms the +3 oxidation state of bismuth [19]. In Figure 3b, the asymmetric peaks observed in the Fe 2p spectrum were resolved into Fe 2p_{3/2} and Fe 2p_{1/2}. The typical peaks of Fe³⁺ were located at 711.03 eV and 724.83 eV, with a satellite peak at 718.22 eV. Meanwhile, the peaks at 709.72 eV and 723.25 eV were assigned to Fe²⁺. The appearance of defects broke the charge balance of the system in the process of Bi ion replacing Gd. In order to make the charge balance of the system, Fe³⁺ ions were converted to Fe²⁺ ions. The presence of Fe ions of varied valence states will be conducive to the formation of more oxygen vacancies, which is beneficial to the surface adsorption on catalysts of organic and oxygen species [20]. Figure 3c depicts the O 1s spectra of the GBFO5 powder; two peaks were found at 529.28 eV and 530.78 eV. The O-I peak is generally believed to be caused by the O²⁻ ion in the crystal structure of the material, and O-II peaks may be formed by oxygen vacancies or defects [21].

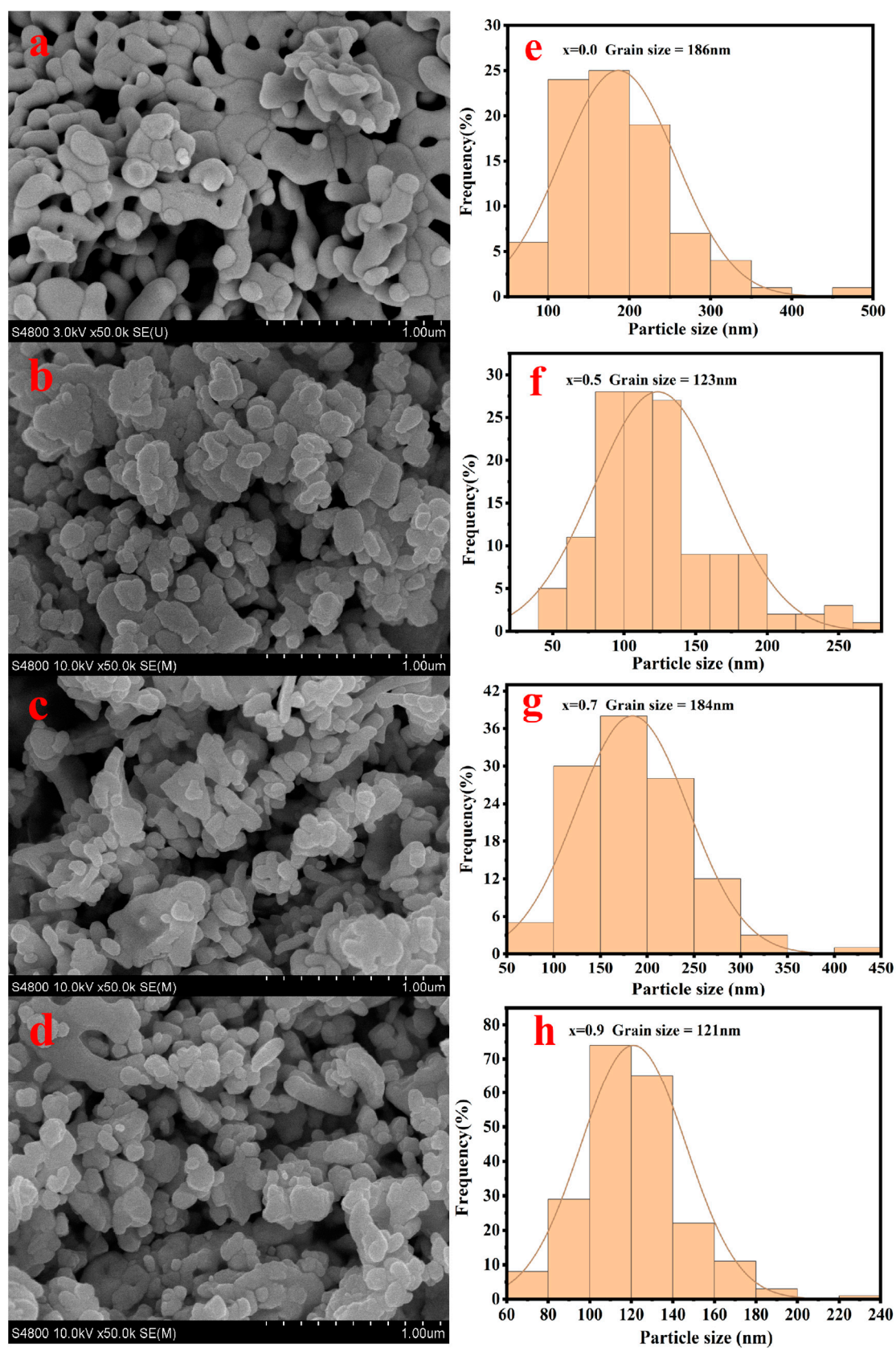


Figure 2. SEM image of (a) GFO calcined at 700 °C; (b) GBFO5 calcined at 700 °C; (c) GBFO7 calcined at 700 °C; (d) GBFO9 calcined at 550 °C; (e–h) statistical estimation of the particle size distribution of GFO, GBFO5, GBFO7 and GBFO9.

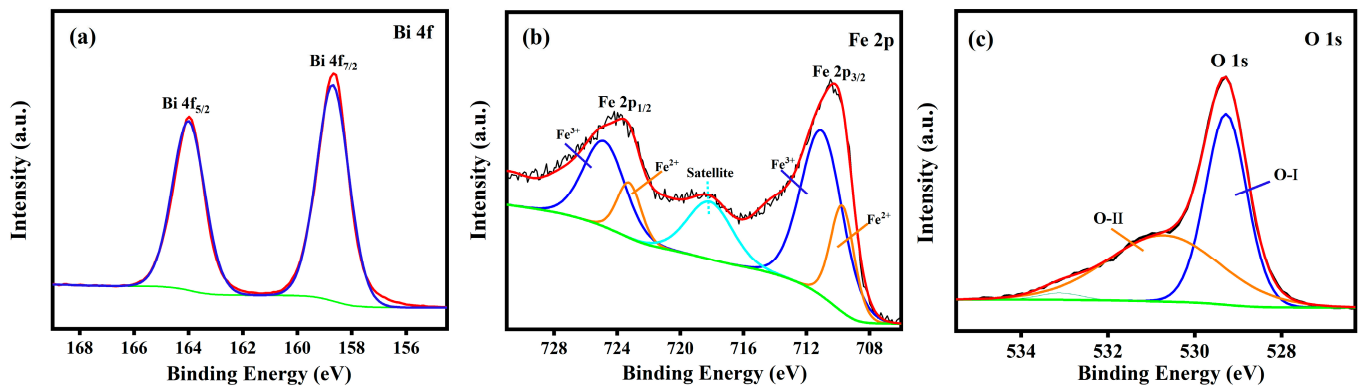


Figure 3. X-ray photoelectron spectroscopy (XPS) spectra of (a) Bi 4f, (b) Fe 2p and (c) O 1s for the $\text{Gd}_{0.5}\text{Bi}_{0.5}\text{FeO}_3$ sample.

Figure 4a,b shows the magnetic hysteresis loops of $\text{Gd}_{1-x}\text{Bi}_x\text{FeO}_3$ ($x = 0.0, 0.1, 0.3, 0.5, 0.7$ and 0.9) at room temperature. In Figure 4a, the linear hysteresis curve was observed for GFO and GBFO1, showing characteristic features of antiferromagnetic (AFM) behavior, due to their canted antiferromagnetic spin structure and high magnetic anisotropic energy. Similar AFM characteristics of GdFeO_3 was also reported by other groups [22,23]. Magnetic hysteresis loops were observed for $\text{Gd}_{1-x}\text{Bi}_x\text{FeO}_3$ ($x = 0.3, 0.5, 0.7, 0.9$), indicating that the weak ferromagnetic behavior was partly induced by Bi^{3+} . Meanwhile, the magnetization was weakened for $\text{Gd}_{1-x}\text{Bi}_x\text{FeO}_3$ ($x = 0.0, 0.1, 0.3, 0.5, 0.7$), and it was moderately strengthened for $\text{Gd}_{1-x}\text{Bi}_x\text{FeO}_3$ ($x = 0.9$) which belongs to the $R3c$ phase of BiFeO_3 . Overall, compared with pure GdFeO_3 , weak ferromagnetic behaviors were observed for solid solution compounds, and the magnetization of $\text{Gd}_{1-x}\text{Bi}_x\text{FeO}_3$ was effectively decreased. In view of the unsaturation of the M-H curves for $\text{Gd}_{1-x}\text{Bi}_x\text{FeO}_3$ ($x = 0-0.7$), canted antiferromagnetic ordering is still considered to exist in these samples even though the ferromagnetism was enhanced.

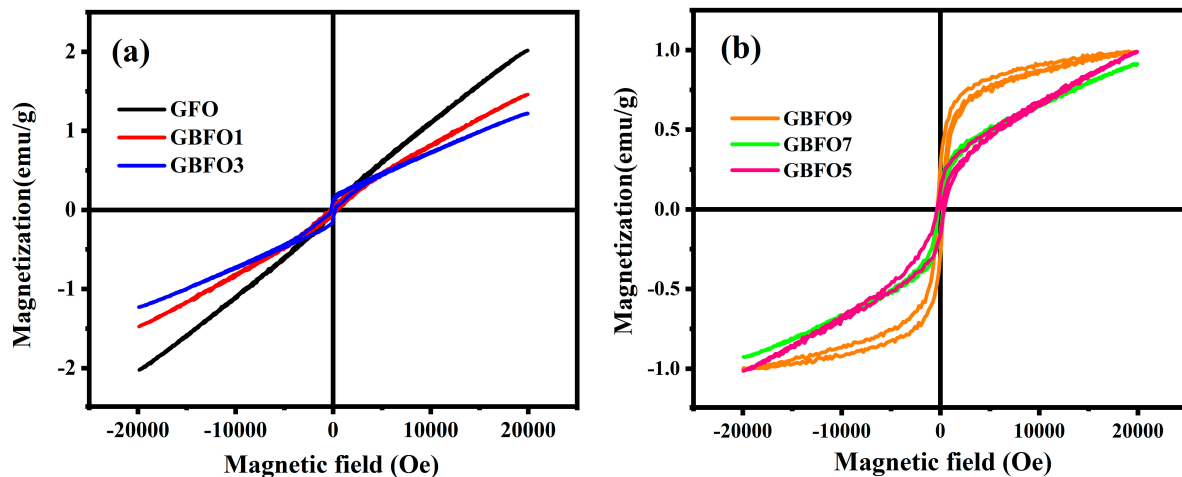


Figure 4. Room temperature magnetic hysteresis loops of (a) GFO, GBFO1 and GBFO3 samples; (b) GBFO5, GBFO7 and GBFO9 samples.

Generally, the magnetic variations are influenced by a variety of factors, including the chemical composition, magnetic anisotropic field, structure, grain size, morphology, defects, domain wall motion, magnetic moment reversal, etc. [24]. With the $Pbnm$ structure, the family of RFeO_3 has two magnetic sublattices from the 4f-electrons of R^{3+} and 3d-electrons of Fe^{3+} , and there exists three types of magnetic exchange interaction: $\text{Fe}^{3+}-\text{Fe}^{3+}$, $\text{R}^{3+}-\text{R}^{3+}$ and $\text{Fe}^{3+}-\text{R}^{3+}$ [1]. The spin-canting of RFeO_3 is mainly caused by the Dzyaloshinskii–Moriya interaction between antiferromagnetically ordered Fe 3d spins, and the spin-canting angle

is closely related to the lattice distortion including the bond angle and length of Fe-O-Fe. For GdFeO₃, at room temperature, the Fe³⁺-Fe³⁺ interaction was dominant, which caused the Fe³⁺ spins usually order at 660 K to have a slightly canted G-type AFM structure. The substitution of Gd³⁺ ions by Bi³⁺ ions with larger radii can result in the modification of the lattice distortion. Considering the XRD refinement results, the Fe-O bond length and the Fe-O-Fe bond angle were highly dependent on the doping content of Bi. It can be seen that magnetization of Gd_{1-x}Bi_xFeO₃ (x = 0, 0.1, 0.3, 0.5, 0.7) was directly proportional to the Fe-O2-Fe bond angle and inversely proportional to the Fe-O2 bond length, which is consistent with the conclusion of Raj et al. [25]. Generally, the introduction of bismuth usually results in decreased magnetization at room temperature, which also originates from decreased interactions between Fe-O-Fe and distortion of the FeO₆ octahedral of the perovskite structure. Meanwhile, according to the SEM results, compared with GFO, smaller and more dispersed particles were observed for Gd_{1-x}Bi_xFeO₃, which possibly led to the enhancement of the surface spin effect, thus reducing the saturation magnetization.

Light absorption is crucial for photocatalytic activities. The UV-vis absorbance spectra of the Gd_{1-x}Bi_xFeO₃ samples are presented in Figure 5. The optical band gap of Gd_{1-x}Bi_xFeO₃ was calculated by the Tauc relationship:

$$(\alpha h\nu) = A(h\nu - E_g)^{\frac{1}{2}} \quad (1)$$

where α , h , ν , E_g and A are the absorption coefficient, Planck's coefficient, light frequency, band gap energy and a constant, respectively. The E_g value was estimated by extrapolating the linear region of the plot in the energy axis (insets in Figure 5). According to linear extrapolation, the bandgap of GdFeO₃ was calculated to be 2.21 eV, which is quite comparable with previous reports [26,27]. For the Bi³⁺-doped GdFeO₃, the optical band gap was effectively decreased, with enhanced absorptions of both UV and visible light. In addition, the narrower band gap allowed more carrier excitation under visible light irradiation, implying improved photocatalytic activities. In particular, the smallest band gap and highest visible light absorption were observed in Gd_{0.5}Bi_{0.5}FeO₃, and the band gap was around 1.8 eV.

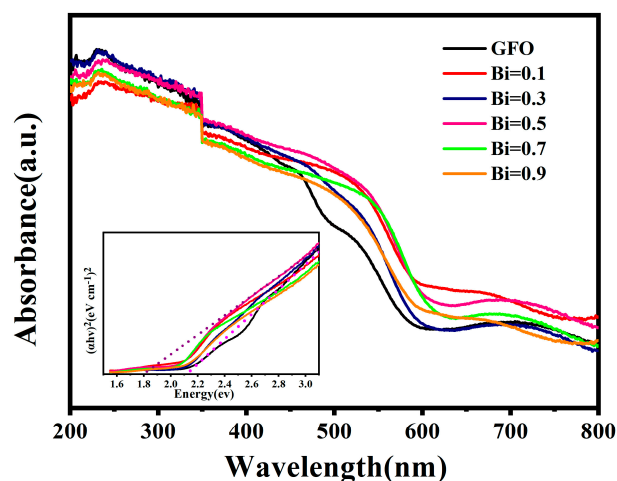


Figure 5. UV-vis absorption spectra of Gd_{1-x}Bi_xFeO₃ nanoparticles; the inset shows the calculation of the band gaps.

In addition, the reduction in band gap for all the doped sample may be related to the distortion in the Fe-O-Fe octahedral rearrangement of molecular orbitals and decreased particles size [28]. The decrease of the band gap was also observed in Sm-doped BiFeO₃ and Mn-doped GdFeO₃ [5,29]. The hybridization between the Fe-3d and O-2p states depends on Fe-O-Fe exchange angles, which directly modify the band gap [14]. In addition, the band gap is also the result of some other factors, such as the defect levels, the crystallinity and

the oxygen vacancies on the surface. Thus, the higher absorption and narrower band gap of GFO5 may originate from its smaller particle size, lattice distortion caused by appropriate Bi ion doping, higher crystallinity, etc. Proper band gap could promote the light absorption and increase photogenerated charge carriers, thus improving the catalytic activity [30]. The introduction of Bi dopants favors the light absorption in the GFO nanoparticles, implying that improved visible light-driven photocatalytic performance is expected.

The photocatalytic activity of $Gd_{1-x}Bi_xFeO_3$ samples were evaluated by degradation of MB under visible light irradiation. The (C_t/C_0) vs. visible light irradiation time (t) curve for $Gd_{1-x}Bi_xFeO_3$ sample is shown in Figure 6a. The concentration of MB hardly changed when the photocatalyst was not added or the reaction was carried out in the dark. It indicates that MB is a stable pollutant and the solution reached the adsorption–desorption equilibrium. After 180 min of visible light illumination, the degradation efficiency reached about 74%, 79.7%, 76.7%, 82.1%, 69% and 63.2% for GFO, GBFO1, GBFO3, GBFO5, GBFO7 and GBFO9, respectively. Obviously, the concentration of Bi^{3+} ions doping affected the photocatalytic performance of the sample. With the increase of the Bi^{3+} doping amount, the degradation efficiency of MB first increased and then decreased, and GBFO5 showed exceptionally enhanced photocatalytic efficiency. The degradation performance of $Gd_{1-x}Bi_xFeO_3$ was similar to the result of the $Y_{1-x}Bi_xFeO_3$ system, in which the catalytic activities ranged from 50% to 80% MB degradation efficiency for 180 min for $x = 0.1$ to $x = 0.4$, respectively [14]. A $BiFeO_3$ - $GdFeO_3$ heterojunction photocatalyst has been reported to degrade 56% MB and 98% MB in 180 min and 9 h, respectively, under sunlight irradiation [31]. The nanogranular $BiFeO_3$ exhibited 53% MB dye degradation after irradiation for 180 min [32]. The nanotubes showed much improved catalytic activity with a degradation efficiency of 75% after irradiation for 180 min. The results also imply that the photocatalytic performance is partly influenced by the crystalline morphology.

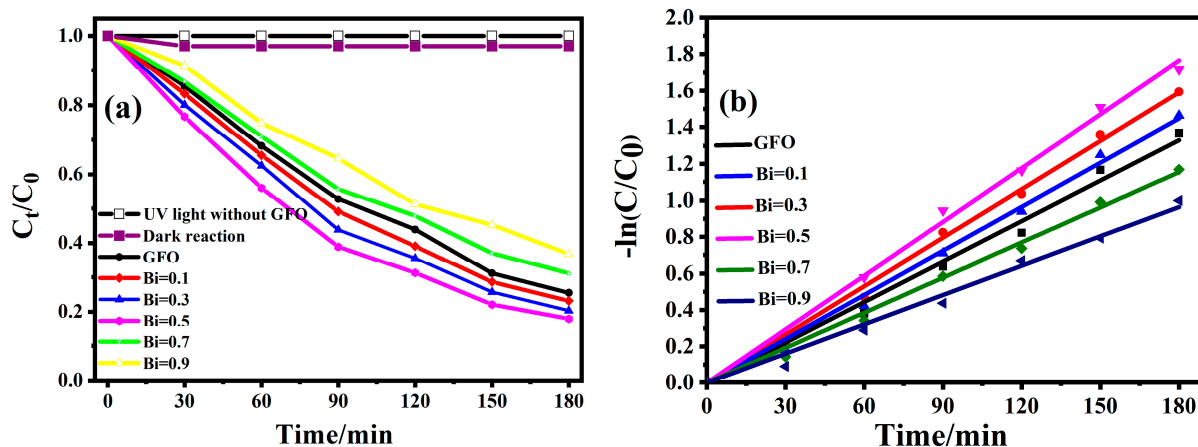


Figure 6. (a) Photocatalytic degradation efficiencies of MB using $Gd_{1-x}Bi_xFeO_3$ as a catalyst; (b) pseudo-first-order kinetics fitting data for the photodegradation of MB over $Gd_{1-x}Bi_xFeO_3$ samples.

Figure 6b represents the $\ln(C_0/C_t)$ vs. irradiation time (t) curves, where the linearity nature indicated the first-order kinetics of the visible light-driven photocatalytic MB degradation. Therefore, the photocatalytic activities can be evaluated by the apparent first-order rate constant k , and it can be expressed by Equation (2) [33]:

$$\ln\left(\frac{C_0}{C}\right) = kt \quad (2)$$

where C_0 represents the initial concentration of MB, C is the concentration of MB after the degradation with respect to time (t) and k is the rate constant. The obtained values of k were $7.3 \times 10^{-3} \text{ min}^{-1}$, $8.0 \times 10^{-3} \text{ min}^{-1}$, $8.8 \times 10^{-3} \text{ min}^{-1}$, $9.8 \times 10^{-3} \text{ min}^{-1}$, $6.4 \times 10^{-3} \text{ min}^{-1}$ and $5.3 \times 10^{-3} \text{ min}^{-1}$ for GFO, GBFO1, GBFO3, GBFO5, GBFO7 and

GBFO9, respectively. This further confirmed that proper Bi^{3+} substitution of GFO can significantly improve the photocatalytic activity.

The charge separation of e^- - h^+ pairs on the interface of the photocatalyst can be revealed by the electrochemical impedance spectra (EIS). The radii of the semicircles are proportional to the charge transfer resistance. For the photocatalytic reaction, a reduction in resistance always means a faster charge transfer and slower recombination of holes and photoelectrons occurred, which is helpful for the relevant photocatalytic efficiency. Figure 7a shows the EIS spectra obtained for GFO, GBFO1, GBFO3, GBFO5, GBFO7 and GBFO9. Compared with GFO, the radius of the semicircle for $\text{Gd}_{1-x}\text{Bi}_x\text{FeO}_3$ ($x = 0.1, 0.3, 0.5$) decreased with increasing Bi^{3+} , implying reduced charge transfer resistance. Thereafter, the radius of the semicircle increased for $\text{Gd}_{1-x}\text{Bi}_x\text{FeO}_3$ ($x = 0.7, 0.9$). GBFO5 exhibited the smallest semicircle, which is indicative of the best charge transfer efficiency and the slowest recombination of holes and photoelectrons out of these five samples, which contribute to the photo-degradation organic pollutants.

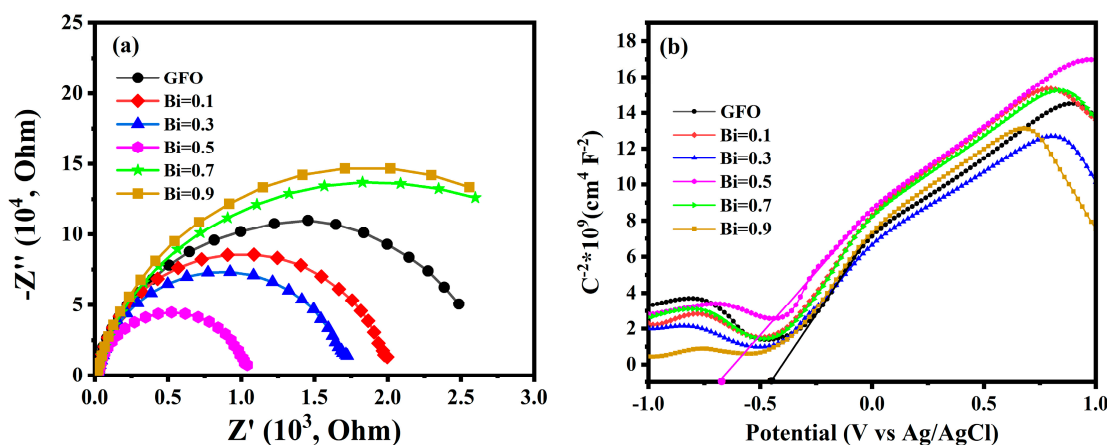


Figure 7. (a) Complex impedance spectra (Z' vs. Z'') and (b) Mott-Schottky plots of $\text{Gd}_{1-x}\text{Bi}_x\text{FeO}_3$ samples at room temperature.

Figure 7b shows the Mott–Schottky plots of GFO, GBFO1, GBFO3, GBFO5, GBFO7 and GBFO9 with a fixed frequency (2000 Hz). The positive slope featured typical n-type semiconductors for the samples. According to Equation (3), the flat band potential V_{FB} of $\text{Gd}_{1-x}\text{Bi}_x\text{FeO}_3$ was estimated by the Mott–Schottky (MS) measurement [34].

$$\frac{1}{C_{sc}^2} = \frac{2}{eN_d\epsilon\epsilon_0} \left(E - E_{\text{FB}} - \frac{KT}{E} \right) \quad (3)$$

where, C_{sc}^2 is the space charge capacitance (in F cm^{-2}), e is electronic charge in C, ϵ_0 is the permittivity of free space, ϵ is the dielectric constant of the semiconductors, N_d is the charge carrier density in cm^{-3} , E_{FB} is the flat band potential in V, K is the Boltzmann constant and T is the temperature in K. The flat-band potentials V_{FB} were obtained from the extrapolation of the Mott–Schottky plots, which were -0.45 , -0.53 , -0.55 , -0.68 , -0.50 and -0.48 eV (vs. Ag/AgCl) for GFO, GBFO1, GBFO3, GBFO5, GBFO7 and GBFO9, respectively. Then, the values corresponded to be -0.25 , -0.33 , -0.35 , -0.48 , -0.30 and -0.28 eV versus the normal hydrogen electrode (NHE), respectively. Generally, the conduction band minimum (E_{CB}) of n-type semiconductors is approximately more negative than E_{FB} by 0.2 eV. Correspondingly, the conduction band minimum (E_{CB}) of $\text{Gd}_{1-x}\text{Bi}_x\text{FeO}_3$ ($x = 0.0, 0.1, 0.3, 0.5, 0.7$ and 0.9) were calculated to be -0.45 , -0.53 , -0.55 , -0.68 , -0.50 and -0.48 eV, respectively. The valence band maximum (E_{VB}) can be determined with the relation $E_g = E_{\text{VB}} - E_{\text{CB}}$, and the optical bandgaps were obtained from the UV-vis absorption spectra. Based on these results, the band energy diagram was displayed in Figure 8.

Compared with GFO, the conduction band of Bi-doped samples was more negative, making it easier to generate superoxide anions to participate in the reactions.

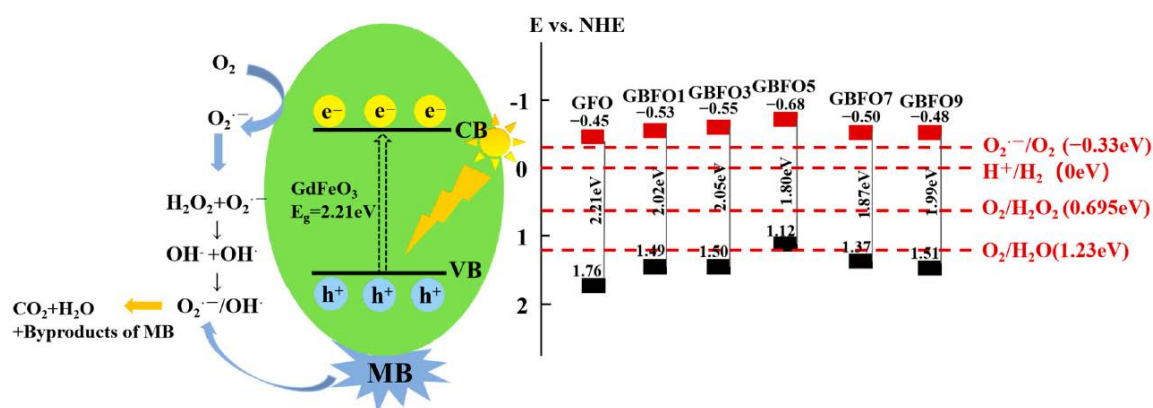
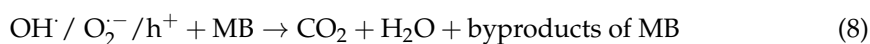
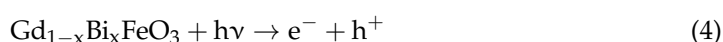


Figure 8. Schematic diagram of the band structure and proposed mechanism of the photocatalytic process.

The scavenger studies were carried out for GBFO5 which was taken as the typical example. Tertbutyl-alcohol (TBA), p-benzoquinone (p-BQ), $K_2Cr_2O_7$ and EDTA-2Na were used as scavengers for $OH\cdot$, $O_2^{\cdot-}$, e^- and h^+ , respectively. These scavengers were separately added to the solution. The photocatalytic experiments were conducted in the presence of the scavengers along with GBFO5. When irradiated for 180 min, with the addition of TBA and EDTA-2Na, the degradation efficiency reached 75.3% and 73.7%, respectively. Compared to the solution without any scavengers, the addition of TBA and EDTA-2Na had a negligible influence on the photocatalytic activity, implying that $OH\cdot$ and h^+ are not the main active species. On the contrary, only 40.2% and 33.7% of MB was degraded with the addition of p-BQ and $K_2Cr_2O_7$, respectively. Severe depression of the performance indicates that $O_2^{\cdot-}$ and e^- were the dominant reactive species responsible for the degradation of MB.

According to the above results and discussions, a possible mechanism of the charge transfer and photocatalytic degradation was also proposed. As illustrated in the scheme in Figure 8, under visible light irradiation, photogenerated electrons in the valence band (VB) of the photocatalyst obtain sufficient energy to jump to the conduction band (CB), leaving holes in the VB (Equation (4)). Since the conduction band edge of $Gd_{1-x}Bi_xFeO_3$ is more negative than the standard redox potential $E(O_2^{\cdot-}/O_2)$ (-0.33 eV vs. NHE) [35], the excited electrons migrate to the catalyst surface, followed by reaction with dissolved O_2 to generate superoxide radicals ($O_2^{\cdot-}$) (Equation (5)). In addition, the standard redox potential $E(O_2/H_2O_2)$ (0.685 eV vs. NHE) [36] is located between the CB and VB of $Gd_{1-x}Bi_xFeO_3$, indicating that electrons could also react with oxygen to form H_2O_2 , which is subsequently reduced to form hydroxyl radicals ($OH\cdot$) (Equations (6) and (7)) [7]. The holes formed at the VB may directly oxidize the organic pollutant [11]. Finally, the superoxide radicals, hydroxyl radical and holes decompose the MB into CO_2 , H_2O and by-products, which could be benzenesulfonic acid 2-amino-5-(methyl amino)-hydroxybenzene sulfonic acid and 2-amino-5-(NN-methyl formamide) benzene sulfonic acid [37].



In addition to the photocatalytic efficiency, the reusability and the stability of photocatalyst are two important factors for practical application. To evaluate the stability, we

conducted photocatalytic experiments using $\text{Gd}_{0.5}\text{Bi}_{0.5}\text{FeO}_3$ for five successive runs under the same conditions as mentioned above. The sample was irradiated for 180 min for every cycle. As shown in Figure 9a, almost no change in the photocatalytic activity was observed after five circulations, suggesting good stability. To further verify its stability, we performed XRD measurements of the GBFO5 nanoparticles before and after the photocatalysis reaction, which is displayed in Figure 9b. The crystal structure of the GBFO5 photocatalyst did not change after the photocatalytic reaction and no secondary phase was observed after the reaction, verifying good stability of this photocatalyst.

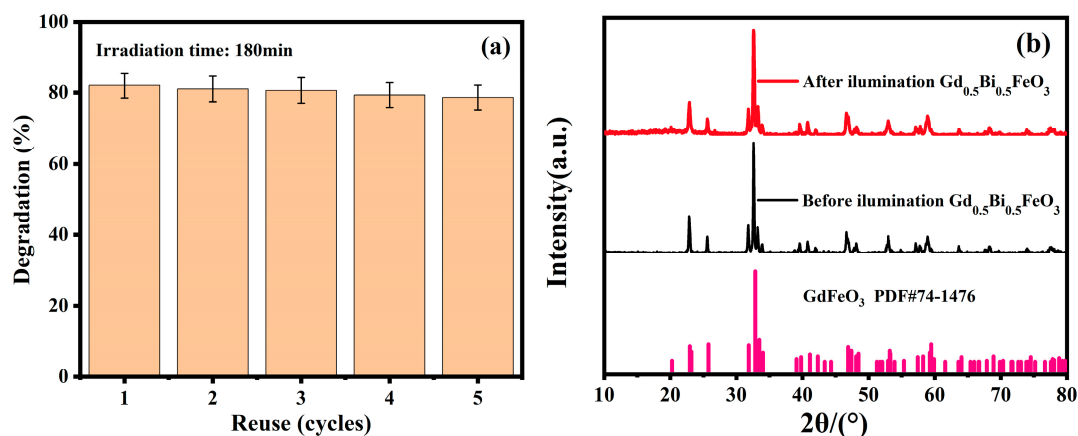


Figure 9. (a) Reusability of $\text{Gd}_{0.5}\text{Bi}_{0.5}\text{FeO}_3$ nanoparticles in the degradation of MB under UV light irradiation over five cycles; (b) XRD patterns of the $\text{Gd}_{0.5}\text{Bi}_{0.5}\text{FeO}_3$ sample before and after the photocatalytic experiment.

The photocatalytic activities are generally determined by numerous factors, including the crystalline phase, morphology, defects, band energy, surface activity, etc. Enhanced photocatalytic activities of $\text{Gd}_{1-x}\text{Bi}_x\text{FeO}_3$ have been observed, with the optimum performance observed with $\text{Gd}_{0.5}\text{Bi}_{0.5}\text{FeO}_3$. The SEM results indicated that GBFO5 samples show smaller particle sizes, which endows it with higher photocatalytic activity due to the increased number of reactive sites for surface reactions. Based on the absorption spectra, it can be seen that Bi doping leads to a lower band gap and higher absorbance in a wider visible light region, which contributed to the generation of more photogenerated carriers. Combined with the EIS and Mott-Schottky measurements, GBFO5 also showed high charge transfer efficiency and more negative redox potential over the $\text{O}_2^{\cdot-}/\text{O}_2$ redox potential. The photogenerated electrons were easier to react with oxygen to generate superoxide anions which were the dominant active species for the degradation of MB. Although GBFO9 was also characterized with smaller crystalline particles, the band structure of GBFO5 is more favorable for the redox reactions. All these factors possibly contribute to the optimum performance of $\text{Gd}_{0.5}\text{Bi}_{0.5}\text{FeO}_3$. Experiments exploring deeper insights into the photocatalytic kinetics are still going on.

4. Conclusions

Polycrystalline nanoparticles of $\text{Gd}_{1-x}\text{Bi}_x\text{FeO}_3$ ($x = 0, 0.1, 0.3, 0.5, 0.7, 0.9, 1$) were successfully synthesized by the sol-gel method. $\text{Gd}_{1-x}\text{Bi}_x\text{FeO}_3$ ($x = 0, 0.1, 0.3, 0.5$) samples maintained the orthorhombic phase (GdFeO_3 , space group $Pbnm$). With further increases of Bi^{3+} , the crystal structure changed to the rhombohedral perovskite (space group $R3c$). Pure GdFeO_3 showed typical antiferromagnetic behavior, and weak ferromagnetism were observed for bismuth-substituted samples with reduced magnetization. The results were explained by the decreased interactions between Fe-O-Fe and distortion of the FeO_6 octahedral of the perovskite structure. Moreover, enhanced photocatalytic activities of $\text{Gd}_{1-x}\text{Bi}_x\text{FeO}_3$ were observed, with the optimum performance observed with $\text{Gd}_{0.5}\text{Bi}_{0.5}\text{FeO}_3$. This behavior could be attributed to reduced particle size, increased UV/visible light absorption,

decreased band gap and higher charge transfer efficiency. Combined with the characteristics of ferromagnetic nature, good stability and reusability, this system is regarded as an excellent candidate for a magnetic photocatalyst, favoring recyclable and reusable applications for the degradation of organic pollutants.

Author Contributions: Conceptualization, H.S.; methodology, Y.M. (Yudie Ma); software, Y.F.; validation, H.G. and Y.L.; formal analysis, Y.Z.; investigation, Y.M. (Yudie Ma); resources, J.X.; data curation, H.S.; writing—original draft preparation, Y.M. (Yudie Ma); writing—review and editing, H.S.; visualization, Y.Z.; supervision, H.S.; project administration, J.X.; funding acquisition, H.S., J.X. and Y.M. (Yunfeng Ma). All authors have read and agreed to the published version of the manuscript.

Funding: This work is supported by the NSAF of China (Grant No. U2130124) and National Natural Science Foundation of China (Grant No. 51972213, No. 51802196).

Conflicts of Interest: The authors declare no conflict of interest.

References

1. Shen, H.; Xian, Q.; Xie, T.; Wu, A.; Wang, M.; Xu, J.; Jia, R.; Kalashnikova, A.M. Modulation of magnetic transitions in SmFeO₃ single crystal by Pr³⁺ substitution. *J. Magn. Magn. Mater.* **2018**, *466*, 81–86. [[CrossRef](#)]
2. Kumar, A.; Sharma, K.; Thakur, M.; Pathania, D.; Sharma, A. Fabrication of high visible light active LaFeO₃/Cl-g-C₃N₄/RGO heterojunction for solar assisted photo-degradation of aceclofenac. *J. Environ. Chem. Eng.* **2022**, *10*, 108098. [[CrossRef](#)]
3. Ismael, M.; Elhaddad, E.; Taffa, D.H.; Wark, M. Synthesis of phase pure hexagonal YFeO₃ perovskite as efficient visible light active photocatalyst. *Catalysts* **2017**, *7*, 326. [[CrossRef](#)]
4. Mengying, X.; Peisong, T.; Junwei, C.; Li, F.; Xinyu, X. Preparation of ErFeO₃ by Sol-gel Method and Its Visible-light Photocatalytic Activity. *Rare Metal. Mat. Eng.* **2018**, *47*, 228–231.
5. Maity, R.; Dutta, A.; Halder, S.; Shannigrahi, S.; Mandal, K.; Sinha, T.P. Enhanced photocatalytic activity, transport properties and electronic structure of Mn doped GdFeO₃ synthesized using the sol-gel process. *PCCP* **2021**, *23*, 16060–16076. [[CrossRef](#)] [[PubMed](#)]
6. Shen, H.; Feng, P.; Jiang, G.; Xian, Q. Synthesis of Mn-doped ErFeO₃ with enhanced photo and vibration catalytic activities. *J. Sol-Gel Sci. Technol.* **2020**, *95*, 230–238. [[CrossRef](#)]
7. Li, L.; Wang, F.; Feng, J.; Guo, S.; Xu, M.; Wang, L.; Quan, G. Step-scheme GdFeO₃/g-C₃N₄ heterostructures with outstanding photocatalytic activity. *J. Mater. Sci.-Mater.* **2021**, *32*, 16400–16410. [[CrossRef](#)]
8. Kebede, M.T.; Devi, S.; Dillu, V.; Chauhan, S. Influence of novel Cd-Ni co-substitution on structural, magnetic, optical and photocatalytic properties of BiFeO₃ nanoparticles. *J. Alloys Compd.* **2022**, *894*, 162552. [[CrossRef](#)]
9. Dumitru, R.; Ianculescu, A.; Păcurariu, C.; Lupa, L.; Pop, A.; Vasile, B.; Surdu, A.; Manea, F. BiFeO₃-synthesis, characterization and its photocatalytic activity towards doxorubicin degradation from water. *Ceram. Int.* **2019**, *45*, 2789–2802. [[CrossRef](#)]
10. Irfan, S.; Zhuanghao, Z.; Li, F.; Chen, Y.X.; Liang, G.X.; Luo, J.T.; Ping, F. Critical review: Bismuth ferrite as an emerging visible light active nanostructured photocatalyst. *J. Mater. Res. Technol.* **2019**, *8*, 6375–6389. [[CrossRef](#)]
11. Kebede, M.T.; Devi, S.; Tripathi, B.; Chauhan, S.; Dillu, V. Structural transition and enhanced magnetic, optical and photocatalytic properties of novel Ce-Ni co-doped BiFeO₃ nanoparticles. *Mater. Sci. Semicond. Process.* **2022**, *152*, 107086. [[CrossRef](#)]
12. Lan, S.; Yu, C.; Sun, F.; Chen, Y.; Chen, D.; Mai, W.; Zhu, M. Tuning piezoelectric driven photocatalysis by La-doped magnetic BiFeO₃-based multiferroics for water purification. *Nano Energy* **2022**, *93*, 106792. [[CrossRef](#)]
13. Mao, Y.; Qiu, J.; Zhang, P.; Fei, Z.; Bian, C.; Janani, B.J.; Fakhri, A. A strategy of silver Ferrite/Bismuth ferrite nano-hybrids synthesis for synergetic white-light photocatalysis, antibacterial systems and peroxidase-like activity. *J. Photoch. Photobiol. A* **2022**, *426*, 113756. [[CrossRef](#)]
14. Rosales-González, O.; Sánchez-De, J.F.; Camacho-González, M.A.; Cortés-Escobedo, C.A.; Bolarin-Miró, A.M. Synthesis of magnetically removable photocatalyst based on bismuth doped YFeO₃. *Mater. Sci. Eng.* **2020**, *261*, 114773. [[CrossRef](#)]
15. Li, J.B.; Rao, G.H.; Xiao, Y.; Liang, J.K.; Luo, J.; Liu, G.Y.; Chen, J.R. Structural evolution and physical properties of Bi_{1-x}Gd_xFeO₃ ceramics. *Acta Mater.* **2010**, *58*, 3701–3708. [[CrossRef](#)]
16. Hu, W.; Chen, Y.; Yuan, H.; Li, G.; Qiao, Y.; Qin, Y.; Feng, S. Structure, magnetic, and ferroelectric properties of Bi_{1-x}Gd_xFeO₃ nanoparticles. *J. Phys. Chem. C* **2011**, *115*, 8869–8875. [[CrossRef](#)]
17. Mahdikhah, V.; Sheibani, S.; Abdi, M. Visible light photocatalytic performance of La-Fe co-doped SrTiO₃ perovskite powder. *Opt. Mater.* **2020**, *102*, 109803.
18. Aamir, M.; Bibi, I.; Ata, S.; Jilani, K.; Majid, F.; Kamal, S.; Alwadai, N.; Raza, M.A.S.; Bashir, M.; Iqbal, S.; et al. Ferroelectric, dielectric, magnetic, structural and photocatalytic properties of Co and Fe doped LaCrO₃ perovskite synthesized via micro-emulsion route. *Ceram. Int.* **2021**, *47*, 16696–16707. [[CrossRef](#)]
19. Patel, S.K.S.; Lee, J.H.; Kim, M.K.; Bhoi, B.; Kim, S.K. Single-crystalline Gd-doped BiFeO₃ nanowires: R3c-to-Pn21 a phase transition and enhancement in high-coercivity ferromagnetism. *J. Mater. Chem. C* **2018**, *6*, 526–534. [[CrossRef](#)]
20. Meng, W.; Hu, R.; Yang, J.; Du, Y.; Li, J.; Wang, H. Influence of lanthanum-doping on photocatalytic properties of BiFeO₃ for phenol degradation. *Chin. J. Catal.* **2016**, *37*, 1283–1292. [[CrossRef](#)]

21. Tong, Z.; Yao, Q.; He, Q.; Deng, J.; Wang, J.; Zhou, H.; Rao, G. Effect of microcosmic regulation of unit cells bonding on microwave absorption properties of perovskite structure GdFeO_3 . *Mater.* **2021**, *20*, 101263. [[CrossRef](#)]
22. Karoblis, D.; Zarkov, A.; Mazeika, K.; Baltrunas, D.; Niaura, G.; Beganskiene, A.; Kareiva, A. YFeO_3 - GdFeO_3 solid solutions: Sol-gel synthesis, structural and magnetic properties. *Solid State Sci.* **2021**, *118*, 106632. [[CrossRef](#)]
23. Mangalmurti, K.; Shirbhate, S.; Acharya, S. Modulation of electric and magnetic ordering in GdFeO_3 orthoferrites system by Ce-doping. *Ferroelectrics* **2022**, *587*, 158–173. [[CrossRef](#)]
24. Akhtar, M.N.; Ali, K.; Umer, A.; Ahmad, T.; Khan, M.A. Structural elucidation, and morphological and magnetic behavior evaluations, of low-temperature sintered, Ce-doped, nanostructured garnet ferrites. *Mater. Res. Bull.* **2018**, *101*, 48–55. [[CrossRef](#)]
25. Raj, R.A.; Meenu, S.; Joseph, A.; Jose, R.; Sajan, D.; Guha, A.; Joy, L.K. Study of the modified magnetic, dielectric, ferroelectric and optical properties in Ni substituted $\text{GdFe}_{1-x}\text{Ni}_x\text{O}_3$ orthoferrites. *Nanotechnology* **2021**, *33*, 035705.
26. Panchwane, A.; Reddy, V.R.; Ajay, G.; Bharathi, A.; Phase, D.M. Study of local distortion and spin reorientation in polycrystalline Mn doped GdFeO_3 . *J. Alloys Compd.* **2018**, *745*, 810–816. [[CrossRef](#)]
27. Ujwal, M.P.; Yashas, S.R.; Shivaraju, H.P.; Swamy, N.K. Gadolinium ortho-ferrite interfaced polyaniline: Bi-functional catalyst for electrochemical detection and photocatalytic degradation of acetaminophen. *Surf. Interfaces* **2022**, *30*, 101878. [[CrossRef](#)]
28. Irfan, S.; Shen, Y.; Rizwan, S.; Wang, H.C.; Khan, S.B.; Nan, C.W. Band-Gap Engineering and Enhanced Photocatalytic Activity of Sm and Mn Doped BiFeO_3 Nanoparticles. *Am. Ceram. Soc.* **2017**, *100*, 31–40. [[CrossRef](#)]
29. Orudzhev, F.F.; Alikhanov, N.M.R.; Ramazanov, S.M.; Sobola, D.S.; Murtazali, R.K.; Ismailov, E.H.; Gasimov, R.D.; Aliev, A.S.; Țălu, S. Morphotropic Phase Boundary Enhanced Photocatalysis in Sm Doped BiFeO_3 . *Molecules* **2022**, *27*, 7029. [[CrossRef](#)] [[PubMed](#)]
30. Wang, X.; Mao, H.; Shan, Y. Enhanced photocatalytic behavior and excellent electrochemical performance of hierarchically structured NiO microspheres. *RSC Adv.* **2014**, *4*, 35614–35619. [[CrossRef](#)]
31. Subramanian, Y.; Ramasamy, V.; Karthikeyan, R.J.; Srinivasan, G.R.; Arulmozhi, D.; Gubendiran, R.K.; Sriramalu, M. Investigations on the enhanced dye degradation activity of heterogeneous BiFeO_3 - GdFeO_3 nanocomposite photocatalyst. *Heliyon* **2019**, *5*, e01831. [[CrossRef](#)] [[PubMed](#)]
32. Li, Y.; Zhang, X.; Chen, L.; Sun, H.; Zhang, H.; Si, W.; Wang, W.; Wand, L.; Li, J. Enhanced magnetic and photocatalytic properties of BiFeO_3 nanotubes with ultrathin wall thickness. *Vacuum* **2021**, *184*, 109867. [[CrossRef](#)]
33. Patil, S.B.; Bhojya Naik, H.S.; Nagaraju, G.; Viswanath, R.; Rashmi, S.K. Synthesis of visible light active Gd^{3+} -substituted ZnFe_2O_4 nanoparticles for photocatalytic and antibacterial activities. *Eur. Phys. Plus* **2017**, *132*, 328. [[CrossRef](#)]
34. Bera, S.; Ghosh, S.; Shyamal, S.; Bhattacharya, C.; Basu, R.N. Photocatalytic hydrogen generation using gold decorated BiFeO_3 heterostructures as an efficient catalyst under visible light irradiation. *Sol. Energy Mater. Sol. Cells* **2019**, *194*, 195–206. [[CrossRef](#)]
35. Wei, K.; Faraj, Y.; Yao, G.; Xie, R.; Lai, B. Strategies for improving perovskite photocatalysts reactivity for organic pollutants degradation: A review on recent progress. *Chem. Eng. J.* **2021**, *414*, 128783. [[CrossRef](#)]
36. Nkwachukwu, O.V.; Muzenda, C.; Ojo, B.O.; Zwane, B.N.; Koiki, B.A.; Orimolade, B.O.; Nkosi, D.; Mabuba, N.; Arotiba, O.A. Photoelectrochemical degradation of organic pollutants on a La^{3+} doped BiFeO_3 perovskite. *Catalysts* **2021**, *11*, 1069. [[CrossRef](#)]
37. Nunocha, P.; Kaewpanha, M.; Bongkarn, T.; Phuruangrat, A.; Suriwong, T. A new route to synthesizing La-doped SrTiO_3 nanoparticles using the sol-gel auto combustion method and their characterization and photocatalytic application. *Mater. Sci. Semicond. Process.* **2021**, *134*, 106001. [[CrossRef](#)]

Disclaimer/Publisher's Note: The statements, opinions and data contained in all publications are solely those of the individual author(s) and contributor(s) and not of MDPI and/or the editor(s). MDPI and/or the editor(s) disclaim responsibility for any injury to people or property resulting from any ideas, methods, instructions or products referred to in the content.